Inorganic Chemistry

pubs.acs.org/IC

Article

Two-Dimensional Hybrid Perovskite with High-Sensitivity Optical Thermometry Sensors

Mengyu Guan, Jiarui Hao, Lei Qiu, Maxim S. Molokeev, Lixin Ning,* Zhigao Dai,* and Guogang Li*

Cite This: https://doi.org/10.1021/acs.inorgchem.3c04140

Read Online

ACCESS | Metrics & More | Article Recommendations | Supporting Information

ABSTRACT: Optical thermometry has gained significant attention due to its remarkable sensitivity and noninvasive, rapid response to temperature changes. However, achieving both high absolute and relative temperature sensitivity in two-dimensional perovskites presents a substantial challenge. Here, we propose a novel approach to address this issue by designing and synthesizing a new narrow-band blue light-emitting two-dimensional perovskite named $(C_8H_{12}NO_2)_2PbBr_4$ using a straightforward solution-based method. Under excitation of near-ultraviolet light, $(C_8H_{12}NO_2)_2PbBr_4$ shows an ultranarrow emission band with the full width at half-maximum (FWHM) of only 19 nm. Furthermore, its luminescence property can be efficiently tuned by incorporating energy transfer from host excitons to Mn^{2+}. This energy transfer leads to dual emission, encompassing both blue and orange emissions, with an impressive energy transfer efficiency of 38.3%. Additionally, we investigated the temperature-dependent fluorescence intensity ratio between blue emission of $(C_8H_{12}NO_2)_2PbBr_4$ and orange emission of Mn^{2+}. Remarkably, $(C_8H_{12}NO_2)_2PbBr_4$:Mn^{2+} exhibited maximum absolute sensitivity and relative sensitivity values of 0.055 K^{-1} and 3.207% K^{-1}, respectively, within the temperature range of 80−360 K. This work highlights the potential of $(C_8H_{12}NO_2)_2PbBr_4$:Mn^{2+} as a promising candidate for optical thermometry sensor application. Moreover, our findings provide valuable insights into the design of narrow-band blue light-emitting perovskites, enabling the achievement of single-component dual emission in optical thermometry sensors.

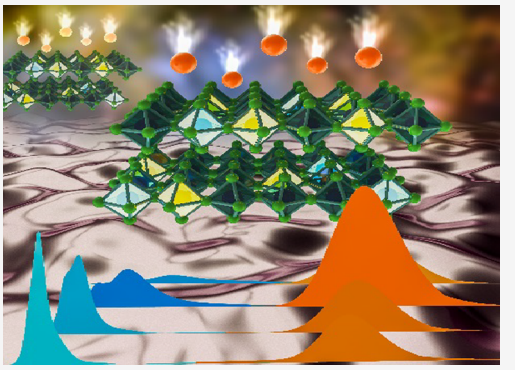

INTRODUCTION

Two-dimensional (2D) organic−inorganic halide perovskites with a layered structure have emerged as promising candidates for fabricating high-performance nanophotonics and optoelectronic devices.[1−5] These perovskites exhibit diverse configurations of organic and inorganic components, thereby expanding the diversity of perovskite material families. The organic components must contain amino groups, and their ionic radius should meet the Goldschmidt tolerance factor.[6] Typically, the organic components in 2D hybrid perovskites are derived from toxic organic reagents such as hexylamine hydrochloride and butylamine hydrochloride. The synthesis of 2D hybrid perovskites using nontoxic, biocompatible, and organic molecules with suitable ionic radii poses a significant challenge. Furthermore, the properties of 2D hybrid perovskites can be effectively optimized by regulating the configuration of the inorganic octahedra units. Divalent manganese (Mn^{2+}), known for its optical activity,[7−10] has been successfully incorporated into 3D perovskite nanocrystals[11−13] and 2D organic−inorganic hybrid perovskites,[7−9,14] to regulate luminous performance associated with $^4T_1$−$^6A1$ transitions of Mn^{2+}. However, previous research has mainly focused on the application of perovskites in light-emitting diodes and β-ray scintillators, with limited exploration of optical temperature sensing based on Mn^{2+}-doped luminescent materials due to the absence of narrow-band 2D organic−inorganic hybrid perovskites.

Commonly used materials for temperature measurements are inorganic luminescent substances, primarily encompassing inorganic phosphors and inorganic metal halide perovskites. The preparation of inorganic phosphors frequently necessitates high-temperature conditions and specific atmospheres. Inorganic metal halide perovskite materials, such as $CsPbX_3$ (X = Cl, Br, and I), display inadequate stability and require sealing within a glass matrix to preserve their superior optical characteristics, which is a factor that contributes to the heightened complexity of the preparation procedure. To propel the advancements in optical thermometric materials even further, it becomes imperative to delve into strategies that not only facilitate facile synthesis but also enable straightforward patterning for practical applications, ultimately leading to the realization of high-sensitivity temperature responses.

Received: November 22, 2023
Revised: January 16, 2024
Accepted: January 23, 2024

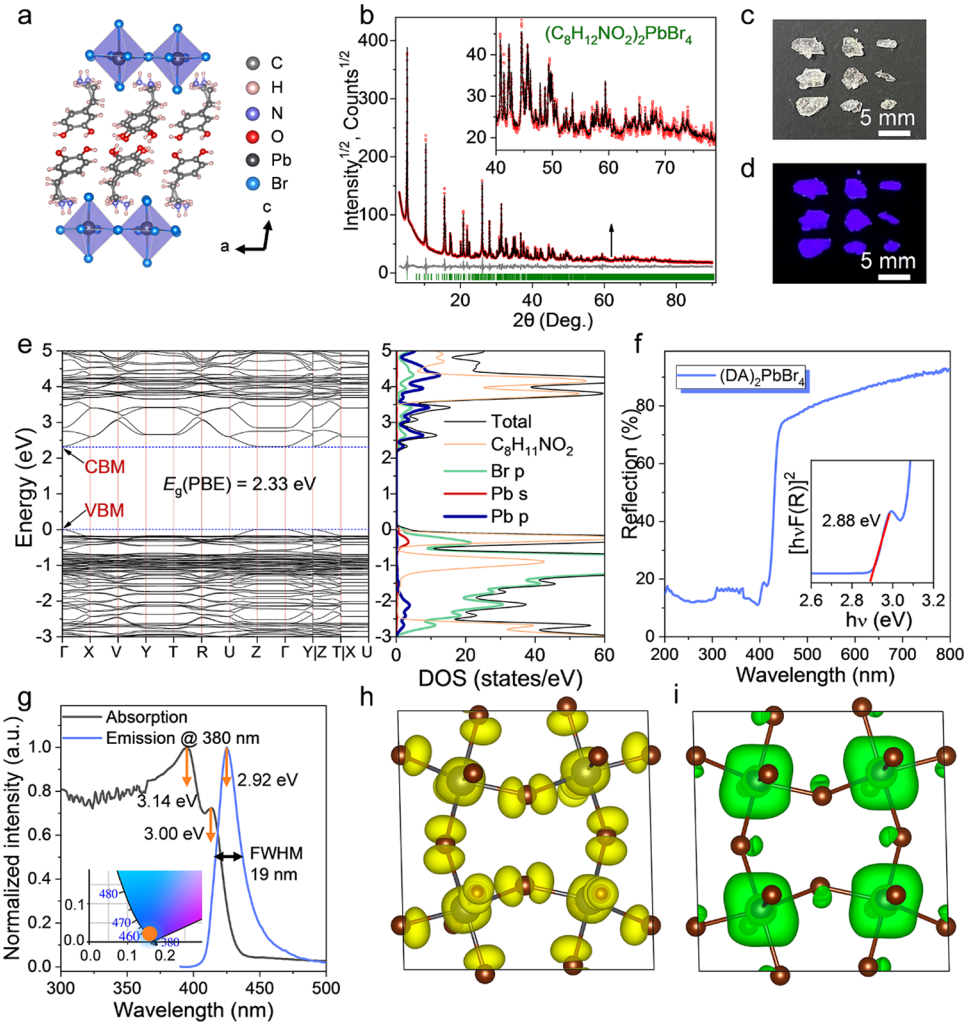

Figure 1. Crystal structure and narrow-band blue emission of $(DA)_2PbBr_4$. (a) Crystal structure of $(DA)_2PbBr_4$. (b) Rietveld refinement results for $(DA)_2PbBr_4$. Photographs of $(DA)_2PbBr_4$ single crystals under (c) daylight illumination and (d) 365 nm UV excitation. (e) Electronic band structure and density of states of $(DA)_2PbBr_4$ calculated using the DFT-PBE method. (f) Diffuse reflectance spectrum of the $(DA)_2PbBr_4$ sample. The inset shows the relationship between $[F(R_\infty)h\nu]^2$ and photon energy $h\nu$. (g) Absorption and PL spectra of $(DA)_2PbBr_4$. The inset shows the CIE chromaticity coordinate diagram for $(DA)_2PbBr_4$. Partial density contours of the hole (h) and the electron (i) wave functions in the relaxed exciton in $(DA)_2PbBr_4$, viewed along the direction of the *c*-axis. The $C_8H_{12}NO_2$ ions are omitted in the figure for clarity.

In this work, we effectively synthesized a novel 2D organic–inorganic hybrid perovskite, $(C_8H_{12}NO_2)_2PbBr_4$ ($(DA)_2PbBr_4$), via a straightforward solution method. This perovskite exhibits narrow-band blue emission with a full width at half-maximum (FWHM) of 19 nm upon excitation with near-ultraviolet light. This narrow-band emission can be attributed to the host excitonic emission, as also confirmed by first-principles calculations. Furthermore, we design an energy transfer from the host to the dopant to achieve dual-color emission of $(DA)_2PbBr_4$. Based on the relationship between fluorescence intensity ratio (FIR) and temperature, maximum absolute sensitivity and relative sensitivity values for $(DA)_2PbBr_4$:Mn^{2+} are 0.055 K^{-1} and 3.207% K^{-1}, respectively. Importantly, we demonstrate the proof-of-concept application of the array display for temperature sensing. This work offers a new perspective on designing novel ultranarrow-band hybrid perovskites and promotes the application of single-component dual-color emitting materials in optical thermometry sensors.

RESULTS AND DISCUSSION

Structure and Luminescent Property of $(DA)_2PbBr_4$. Single crystals were obtained by using a simple room-temperature crystallization method. They were grown from a hydrobromic acid solution, which was slowly cooled and then subjected to recrystallization (for details, see the Experimental Section/Methods). The crystal structure was determined by using single-crystal X-ray diffraction (SCXRD) analysis. The experimental results revealed that the single crystal corresponds to a 2D organic–inorganic hybrid metal halide perovskite, specifically $(DA)_2PbBr_4$, and its crystal structure is depicted in Figure 1a. The obtained single crystal crystallizes in the triclinic crystal system with a space group of *P-1*. The unit cell parameters are as follows: a = 11.4417, b = 11.6210, c = 17.5700 Å, α = 99.5680°, β = 98.6950°, γ = 90.0010°. The $(DA)_2PbBr_4$ crystal exhibits a characteristic 2D-layered structure consisting of alternately arranged organic layers $(C_8H_{12}NO_2)^+$ (Figure S1a) and the corner-sharing inorganic layer $[PbBr_6]^{4-}$ (Figure S1b) in the form of octahedra. The structural analysis reveals the presence of hydrogen bonds that

https://doi.org/10.1021/acs.inorgchem.3c04140
Inorg. Chem. XXXX, XXX, XXX−XXX

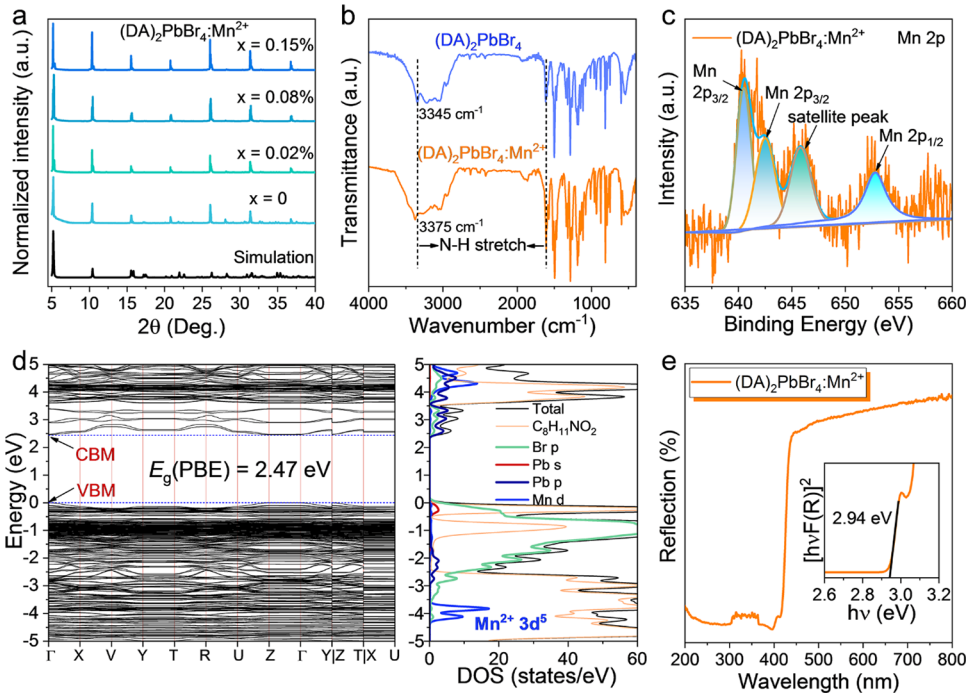

Figure 2. Doping effect on narrow-band blue emission of $(DA)_2PbBr_4$. (a) XRD patterns of $(DA)_2PbBr_4$:Mn^{2+} at different Mn^{2+} concentrations. (b) FTIR spectra of $(DA)_2PbBr_4$ and $(DA)_2PbBr_4$:0.15%Mn^{2+}. (c) High-resolution XPS spectra of Mn 2p. (d) Electronic band structure and DOSs of $(DA)_2PbBr_4$:Mn_{Pb1} calculated using the DFT-PBE method. (e) Diffuse reflectance spectra of the $(DA)_2PbBr_4$:Mn^{2+} sample. The inset shows the relationship between $[F(R_\infty)h\nu]^2$ and photon energy $h\nu$.

connect the organic molecules to the corner-sharing inorganic octahedra $[PbBr_6]^{4-}$, forming a three-dimensional network. The crystallographic information for $(DA)_2PbBr_4$ is provided in the Supporting Information. The Rietveld refinement of the powder XRD data is presented in Figure 1b. The main crystal data, atom coordinates, and primary bond lengths are presented in Tables S1, S2, and S3, respectively. Additionally, the XRD pattern of $(DA)_2PbBr_4$ exposed to air for 4 months remains consistent with that of the fresh sample (Figure S2), indicating the good ambient stability of $(DA)_2PbBr_4$.

The photographs taken under daylight (Figure 1c) and 365 nm ultraviolet (UV) light (Figure 1d) reveal that the synthesized single crystals, with a crystal size of approximately 5 mm, exhibit blue light emission. When observed under a fluorescence microscope, $(DA)_2PbBr_4$ appears as a lamellar structure, exhibiting a bluish glow (Figure S3). Additionally, the microstructure of $(DA)_2PbBr_4$ was examined by using high-resolution transmission electron microscopy (HRTEM) and element mapping. The HRTEM image (Figure S4) displays distinct lattice fringes corresponding to the crystallographic plane (222) of triclinic phase, indicating good crystallinity. The elemental mapping images for C, N, O, Pb, and Br demonstrate their homogeneous distribution within $(DA)_2PbBr_4$ (Figure S5).

The electronic band structure, total density of states (DOS), and orbital-projected DOSs of the $(DA)_2PbBr_4$ unit cell were calculated using the density functional theory (DFT) approach with the Perdew–Burke–Ernzerhof (PBE) functional[15] (Figure 1e). The calculated results reveal a direct band gap of 2.33 eV, with the valence band maximum and conduction band minimum at the k-point Γ. It should be noted that the band gap is underestimated when the DFT-PBE method. The top valence band is composed of antibonding orbitals between Pb $6s^2$ lone pair and Br-4p orbitals, while the bottom conduction band is relatively more dispersive and consists of antibonding orbitals involving the Pb-6p and Br-4p orbitals. The dispersion arises from the electronic coupling between $[PbBr_6]^{4-}$ octahedra in the layered structure and often results in the formation of mobile excitons, which facilitate energy transfer from excitons to the dopants.

To gain further insights into the absorption properties, we measured the experimental optical band gap of $(DA)_2PbBr_4$ by using diffuse reflectance spectroscopy (Figure 1f). The optical band gap of $(DA)_2PbBr_4$ is determined using the Kubelka–Mun equation:[16]

$$F(R) = (1 - R)^2/2R \quad (1)$$

$$[F(R)h\nu]^n = D(h\nu - E_g) \quad (2)$$

where R represents the reflectance coefficient (%), $h\nu$ is the photon energy, D is the absorption constant, E_g is the optical band gap. The inset in Figure 1f reveals that the experimental optical band gap of $(DA)_2PbBr_4$ is 2.88 eV, slightly higher than the calculated band gap, which is likely attributed to an inherent deficiency of the computation method.

In order to further investigate the optical properties of $(DA)_2PbBr_4$ experimentally, the absorption spectrum of $(DA)_2PbBr_4$ at room temperature reveals two closely spaced excitonic peaks at approximately 395 (3.14) and 413 nm (3.00 eV). Additionally, upon 380 nm excitation, the material displays a narrow-band emission at 425 nm (2.92 eV) with an FWHM of 19 nm (Figure 1g). These characteristics are typical of 2D hybrid perovskites, and the narrow-band emission can be attributed to the host excitonic emission.[17,18] The wavelength-dependent spectra of photoluminescence excitation (PLE) and photoluminescence emission (PL) of $(DA)_2PbBr_4$ further confirm that the luminescence is attributed to the host excitonic emission (Figures S6 and S7).

https://doi.org/10.1021/acs.inorgchem.3c04140
Inorg. Chem. XXXX, XXX, XXX−XXX

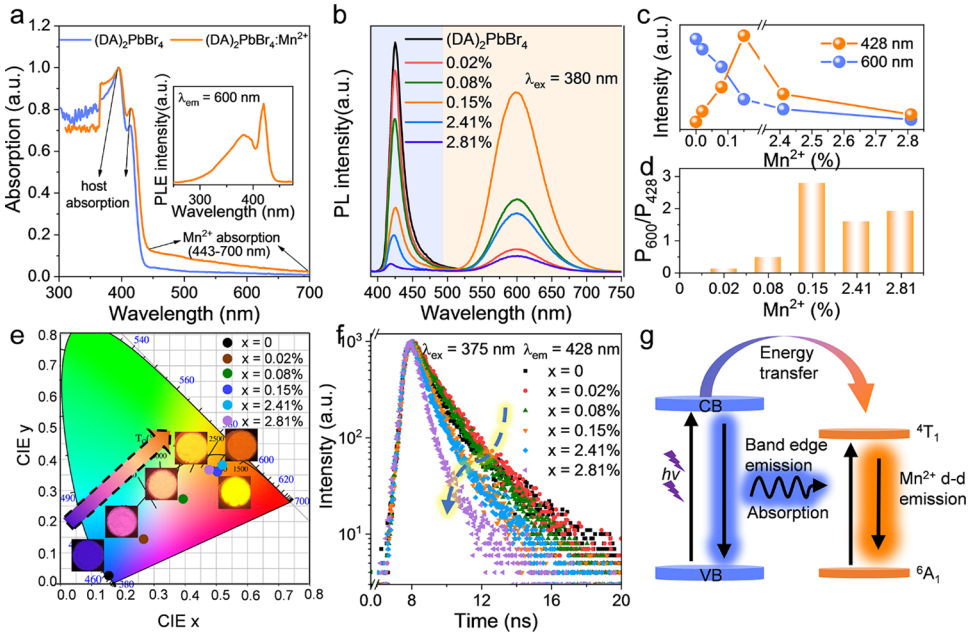

Figure 3. Efficient energy transfer in the narrow-band blue emission of $(DA)_2PbBr_4$. (a) Absorption spectra of $(DA)_2PbBr_4$:$x$$Mn^{2+}$ (x = 0, 0.15%). (b) PL spectra of the $(DA)_2PbBr_4$:$x$$Mn^{2+}$ samples under 380 nm excitation. (c) Variations of the intensities of peak 1 (428 nm, blue line) and peak 2 (600 nm, orange line) with increasing Mn^{2+} content. (d) Relative peak intensity ratio of P_{600}/P_{428} as a function of Mn^{2+} concentration under the excitation wavelength of 380 nm. (e) CIE chromaticity coordinate diagram of $(DA)_2PbBr_4$:$x$$Mn^{2+}$ under 380 nm excitation and corresponding luminescence photographs under 365 nm UV light. (f) PL decay curves of $(DA)_2PbBr_4$:$x$$Mn^{2+}$ under excitation at 375 nm, monitored at 428 nm. (g) Scheme showing the mechanism of energy transfer in $(DA)_2PbBr_4$:Mn^{2+} perovskite.

In order to provide further evidence for the aforementioned assignment, we employed DFT with the hybrid PBE0 functional[19] to calculate the excitonic absorption and emission energies of $(DA)_2PbBr_4$. This functional has also been utilized in theoretical investigation of excitons in other hybrid perovskite materials.[20] The calculated values for the lowest excitonic absorption energy and excitonic emission energy are 3.09 and 2.81 eV, respectively, which closely align with the experimental values (3.00 and 2.92 eV, respectively). Moreover, the calculated binding energy of the relaxed exciton structure is 0.92 eV, which is sufficiently large to ensure strong excitonic absorption and luminescence features observed in this work.[18] Figure 1h,i illustrates the calculated partial density contours of the hole and electron wave functions in the relaxed exciton, revealing that the hole and electron states correspond to the Pb-6s-Br-4p- and Pb-6p-Br-4p-hybridized orbitals, respectively.

Efficient Energy Transfer Based on $(DA)_2PbBr_4$. To manipulate the narrow-band blue emission of $(DA)_2PbBr_4$, we introduced Mn^{2+} as a partial replacement for Pb^{2+}. First, the precise doping content of Mn^{2+} was measured using an inductively coupled plasma optical emission spectrometer. The actual Mn^{2+} ratios in the Mn^{2+}-doped $(DA)_2PbBr_4$ samples, prepared with $MnBr_2$ concentrations of 10%, 30%, 50%, 70%, and 90%, were estimated to be 0.02%, 0.08%, 0.15%, 2.41%, and 2.81%, respectively, indicating successful Mn^{2+} doping in $(DA)_2PbBr_4$.

Subsequently, the phase of $(DA)_2PbBr_4$:$x$$Mn^{2+}$ (x is the actual ratio of Mn^{2+}) was characterized using XRD. The XRD patterns of $(DA)_2PbBr_4$:$x$$Mn^{2+}$ with various Mn^{2+} concentrations are shown in Figure 2a, revealing that both pure and Mn^{2+}-doped $(DA)_2PbBr_4$ samples exhibit a single phase and display the typical diffraction peaks of 2D-layered perovskite.

Importantly, the diffraction peaks of Mn^{2+}-doped $(DA)_2PbBr_4$ do not shift toward higher or lower diffraction angle, suggesting minimal alteration in the original crystal structure upon Mn^{2+} doping. Furthermore, Figure S8 presents elemental mapping images of Br, Pb, and Mn, demonstrating their homogeneous distribution within the material. Fourier transform infrared (FTIR) spectroscopy was conducted to investigate the changes in the environment of the amine group ligand following Mn^{2+} doping (Figure 2b).

A comparison between DA_2PbBr_4 and Mn^{2+}-doped $(DA)_2PbBr_4$ revealed a shift in the peak associated with the amino group of DA^+. Specifically, the N−H scissor peak shifted from 1616 to 1610 cm^{-1}, while the N−H stretch peak shifted from 3345 to 3375 cm^{-1}. These observations indicate a change in the chemical environment of amine group in DA_2PbBr_4 changes after Mn^{2+} doping.[8,21,22]

To further confirm the effect of Mn^{2+} introduction in $(DA)_2PbBr_4$, X-ray photoelectron spectroscopy (XPS) spectra of pure and Mn^{2+}-doped $(DA)_2PbBr_4$ were characterized (Figures 2c and S9). As shown in Figure S8, the XPS spectra exhibit signals corresponding to C 1s, N 1s, Pb 4f, Br 3d, and Mn 2p. In the high-resolution XPS spectrum of Mn 2p (Figure 2d), two peaks at 640.5 and 642.5 eV correspond to Mn $2p_{3/2}$, while a peak at 652.8 eV corresponds to Mn $2p_{1/2}$, confirming the successful doping of Mn^{2+} in $(DA)_2PbBr_4$. Additionally, high-resolution XPS spectra of Br 3d and Pb 4f signals were obtained to demonstrate the presence of Mn^{2+} in Mn^{2+}-doped $(DA)_2PbBr_4$. In the Br 3d XPS spectrum (Figure S9b), the binding energy of Br 3d shifts to a higher energy upon Mn^{2+} introduction, indicating a change in the chemical bond between Pb^{2+} and Br^-. Interestingly, the Pb 4f peaks do not shift with Mn^{2+} doping, suggesting the incorporation of Mn^{2+} into the $(DA)_2PbBr_4$ perovskite structure (Figure S9c).

https://doi.org/10.1021/acs.inorgchem.3c04140
Inorg. Chem. XXXX, XXX, XXX−XXX

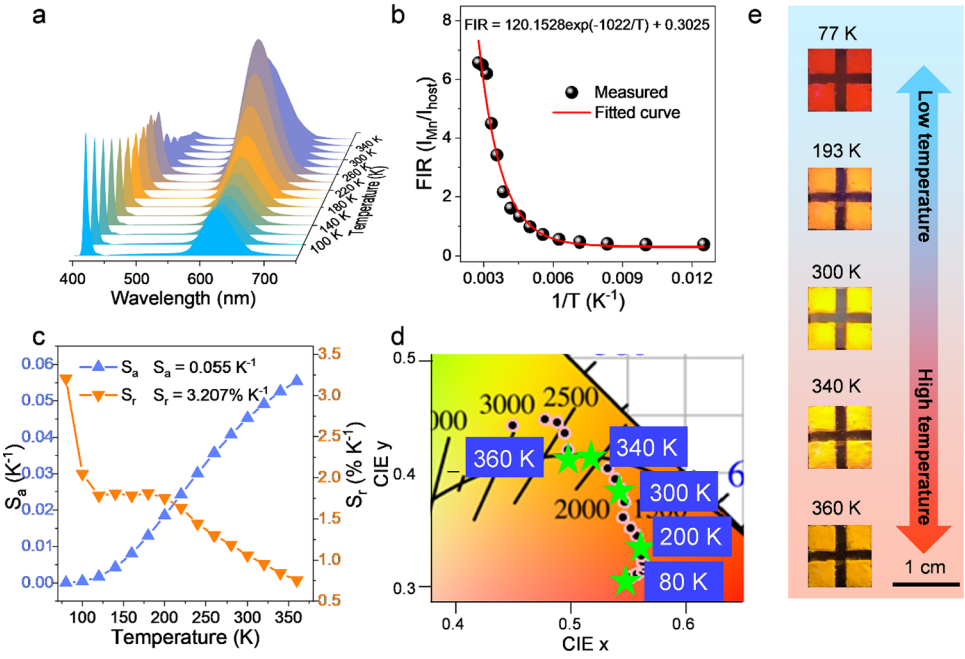

Figure 4. Temperature sensing performance of the narrow-band blue emission of $(DA)_2PbBr_4$. (a) Temperature-dependent emission spectra of $(DA)_2PbBr_4$:Mn^{2+} samples. (b) Histogram of the emission intensity for the host peak (428 nm) and Mn peak (600 nm) of $(DA)_2PbBr_4$:0.15% Mn^{2+} excited. (b) FIR (I_{Mn}/I_{host}) at different temperatures and the fitted result. (c) Absolute sensitivity value S_a and relative sensitivity value S_r calculated at different temperatures. (d) Visualization luminescence photographs of the studied $(DA)_2PbBr_4$:Mn^{2+} samples upon 77, 193, 300, 340, and 360 K. (e) CIE chromaticity coordinate diagram of $(DA)_2PbBr_4$:Mn^{2+} under 380 nm excitation with the temperature rising from 80 to 360 K.

There are two crystallographically distinct Pb sites in $(DA)_2PbBr_4$. DFT total energy calculations indicate that Mn^{2+} substitutes for the two Pb sites with nearly equal probabilities. Hereafter, the Mn site occupation at Pb1 or Pb2 site will not be differentiated unless otherwise specified. Figure 2d illustrates the electronic band structure, total DOS, and orbital-projected DOS of the $(DA)_2PbBr_4$ unit cell with Mn substituting at the Pb1 site. The results for the unit cell with Mn substituting at the Pb2 site are nearly identical (Figure S10). The Mn^{2+} $3d^5$ orbitals are found deep within the valence band and split into two bands due to their interaction with the octahedral ligand field. This observation suggests that the Mn^{2+} $3d^5$ states are highly localized, making them charge-stable activators in the host material. Furthermore, Mn doping leads to a slight increase in the band gap compared to that of the host material (2.47 vs 2.33 eV in Figure 1e). This widening is attributed to an upward shift of the conduction band caused by the hybridization of Mn 3d orbitals with Br 4p orbitals. Experimentally, the band gap of $(DA)_2PbBr_4$:Mn^{2+} (2.94 eV in Figure 2e) is slightly larger than that of the host material (2.88 eV in Figure 1f), which is consistent with the theoretical calculations.

In investigate the impact of Mn^{2+} doping on photoluminescence properties and mechanism, ultraviolet−visible light (UV−vis) absorption spectra, PLE, PL, decay curves, and time-resolved PL spectra were measured. Figure 3a displays the room-temperature UV−vis absorption spectra of $(DA)_2PbBr_4$:xMn^{2+} (x = 0, 0.15%). The prominent absorption peaks at approximately 395 nm and 414 nm are assigned to the absorption of the host material. Weak Mn^{2+} absorption in 443−700 nm region was observed in $(DA)_2PbBr_4$:0.15% Mn^{2+},[23] indicating a minimal impact of Mn dopants on the electronic structure of the $(DA)_2PbBr_4$ host due to the spin forbidden transition.[24]

The PLE and PL spectra (Figures 3b and S11 and S12) reveal that Mn^{2+}-doped $(DA)_2PbBr_4$ exhibits tunable dual-color emission (blue and orange emission), with blue emission attributed to the host band edge (428 nm, peak 1) and orange emission attributed to Mn^{2+} d−d transition (600 nm, peak 2).

With the Mn^{2+} doping concentration from 0 to 0.15%, the intensity of peak 1 gradually decreases, while the intensity of peak 2 increases (Figures 3c,d and S13). This change is attributed to efficient energy transfer from host to Mn^{2+}. In the range of Mn^{2+} doping concentration from 0.15 to 2.81%, the intensity of Mn^{2+} d−d emission gradually decreases due to concentration quenching. Overall, the emission of $(DA)_2PbBr_4$:Mn^{2+} can be tuned by varying the Mn^{2+} concentration. Figure 3e displays the CIE chromaticity coordinate diagram of $(DA)_2PbBr_4$:xMn^{2+} under 380 nm excitation. The color coordinates of $(DA)_2PbBr_4$:xMn^{2+} shift from (0.1605, 0.0276) to (0.4819, 0.3639) as the x increases from 0 to 2.81%. Additionally, the corresponding luminescence photographs of $(DA)_2PbBr_4$:xMn^{2+} samples are presented under 365 nm UV light, clearly demonstrating the tunability of emission colors.

Additionally, to confirm the presence of multiple luminescence centers and gain insights into the photophysical process, we measured the PL decay curves of $(DA)_2PbBr_4$:xMn^{2+} at various monitoring wavelengths. We monitored the PL decay curves under excitation at 380 nm and emission at 600 nm, which were accurately fitted using a monoexponential model (Figure S14). The measured lifetime values were determined to be 0.41 ms, corresponding to the $^4T_1$−$^6A_1$ transition of Mn^{2+} and consistent with the previous reports in Mn-doped metal halides.[9] Figure 3f illustrates the PL decay curves obtained under excitation at 375 nm and emission at 428 nm, which were well-fitted using monoexponential function. The calculated average lifetime values, ranging from 0.64 to 1.50 ns,

https://doi.org/10.1021/acs.inorgchem.3c04140
Inorg. Chem. XXXX, XXX, XXX−XXX

are attributed to the host excitonic emission of the $(DA)_2PbBr_4$:Mn^{2+} and are listed in Table S4. Increasing the doping concentration of Mn^{2+} leads to a decrease in the lifetime of the excitonic emission, indicating the presence of an energy-transfer process in $(DA)_2PbBr_4$:Mn^{2+}. Furthermore, the energy transfer efficiency (η) between the host and Mn^{2+} was calculated using the following equation, based on the PL decay curves:[25]

$$\eta = 1 - \frac{\tau_s}{\tau_{s0}} \tag{3}$$

where τ_s and τ_{s0} represent the luminescence lifetimes with and without Mn^{2+}, respectively. Figures 3f and S15 indicate a gradual improvement in η value with increasing Mn^{2+} doping concentration, with the maximum value reaching 38.3% at x = 2.81%. Based on the above discussion, the schematic energy transfer diagram of the luminescence process in $(DA)_2PbBr_4$:Mn^{2+} is described in Figure 3g, demonstrating the free excitons and Mn^{2+} d states in $(DA)_2PbBr_4$:Mn^{2+}. Under UV light excitation, free excitons are generated, which leads to narrow-band blue emission of nontonxic dopmaine-based $(DA)_2PbBr_4$. Along with Mn^{2+} doping, the energy transfer of the free excitons to Mn^{2+} d states arises, which causes Mn^{2+} d−d emission.[26] The dual-color emission (blue and orange emission) of $(DA)_2PbBr_4$:Mn^{2+} could be a candidate for high-sensitivity optical theremometry sensors.

High-Sensitivity Optical Thermometry Sensors Based on Dual-Color-Emitting $(DA)_2PbBr_4$:Mn^{2+}. Based on the host exciton emission and d−d characteristic emission of Mn^{2+}, the temperature sensing properties of $(DA)_2PbBr_4$:Mn^{2+} were explored. The temperature-dependent PL spectra of $(DA)_2PbBr_4$:0.15%Mn^{2+} in the range 80−360 K are shown in Figure 4a. The host emission decreases, while the Mn^{2+} emission increases as the temperature rises from 80 to 260 K (Figures S15−S17), due to energy transfer from host to Mn^{2+}. Moreover, the lifetime of host emission decreases with increasing temperature, indicating an increase in energy transfer efficiency from host to Mn^{2+} (Figure S19 and Table S5). The Mn^{2+} emission decreases as the temperature increases from 260 to 360 K, due to the effect of concentration quenching.

The temperature sensitivity of $(DA)_2PbBr_4$:0.15%Mn^{2+} for optical thermometry was evaluated using the luminescent performance of $(DA)_2PbBr_4$:0.15%Mn^{2+} perovskite and the Struck and Fonger theory. The relationship[27] between temperature and the emission peak intensity of host (I_{host}) and Mn^{2+} (I_{Mn}) is expressed as shown in Figures 4b and S20:

$$\mathrm{FIR} = \frac{I_{Mn}}{I_{host}} = A\exp(-\Delta E/k_B T) + B \tag{4}$$

where A and B are related proportional parameter, ΔE is the energy gap between the two coupled states, k_B is the Boltzmann constant, and T is the absolute temperature. Additionally, the absolute sensitivity S_a and relative sensitivity S_r can be described by the following equations:[28]

$$S_a = \frac{d\mathrm{FIR}}{dT} = C\exp\left(-\frac{\Delta E}{k_B T}\right) \times \frac{\Delta E}{k_B T^2} \tag{5}$$

$$S_r = 100\% \times \left|\frac{1}{\mathrm{FIR}}\frac{d\mathrm{FIR}}{dT}\right| = 100\% \times \frac{C\exp(-\Delta E/k_B T)}{D + C\exp(-\Delta E/k_B T)} \times \frac{\Delta E}{k_B T^2} \tag{6}$$

where C and D are related parameters.

The S_a and S_r of $(DA)_2PbBr_4$:0.15%Mn^{2+} calculated by eqs 5 and 6 are shown in Figure 4c. The maximum values of S_a and S_r are 0.055 K^{-1} and 3.207% K^{-1}, respectively. Additionally, the maximum values of S_a and S_r are 0.107 K^{-1} and 1.009% K^{-1} by calculating the relationship between the PL integrated intensity and temperature (Figure S21). Comparative analysis with previously documented temperature sensors (Table 1) revealed that $(DA)_2PbBr_4$:Mn^{2+} not only demonstrates a relatively high relative sensitivity, comparable to $Y_3Al_5O_{12}$:Eu^{3+}/Mn^{4+}, but also stands as an example of a 2D organic−inorganic hybrid perovskite material for temperature sensing, offering potential advantages in terms of facile synthesis.

Table 1. Maximum Absolute and Relative Sensitivities of Representative Temperature Sensing Materials in Previous Reports

Materials	S_a (K^{-1})	S_r (%K^{-1})	Range (K)	Ref.
$SrTiO_3$:Er^{3+}/Yb^{3+}	0.0124	No	300−500	29
$BaTiO_3$:Ho^{3+}/Yb^{3+}	No	2.78	298−578	30
$Y_3Al_5O_{12}$:Eu^{3+}/Mn^{4+}	0.441	4.81	293−393	31
$CsPbBr_3/EuPO_4$	0.082	1.80	303−483	32
GdF_3:Ce^{3+}/Mn^{2+}/Eu^{3+}	0.078	1.32	298−433	33
$CsPbBr_3$:Eu^{3+}	0.0224	2.25	93−383	34
$CsPbCl_2Br$:Eu^{3+}	0.0315	3.097	80−440	35
$CsPbI_3$:Tb^{3+}	0.034	1.78	80−480	36
$(TTPhP)_2MnCl_4$:Sb^{3+}	0.236	3.77	300−400	37
$(DA)_2PbBr_4$:Mn^{2+}	0.055	3.207	80−360	This work

Figure 4d illustrates the fluorescent photographs of the "2 × 2 array" taken under 365 nm UV light, showing the transition from low to high temperature. The "2 × 2 array" exhibited a transition from orange-red light to yellow light with an increase in temperature under UV light excitation. In addition, as seen from the CIE (Figure 4e), the luminescent color transitions from orange-red to yellow as the temperature increased from 77 to 360 K.

CONCLUSIONS

In summary, we have successfully developed a novel 2D hybrid halide perovskite with narrow-band blue emission based on the nontoxic biocompatible dopamine molecule ($C_8H_{11}NO_2$). Notably, we have achieved the construction of a high-sensitivity optical thermometry sensor in an organic−inorganic hybrid context. Through strategic design, we have enabled energy transfer from the host excitons to Mn^{2+} dopants, thereby achieving dual-emission capabilities in the $(DA)_2PbBr_4$:Mn^{2+} 2D organic−inorganic hybrid perovskite. By adjusting the dopant concentration, we can precisely control the fluorescence colors, ranging from blue to orange. Strong experimental and theoretical support confirms the presence of energy transfer in $(DA)_2PbBr_4$:xMn^{2+} ($0 \le x \le 2.81\%$), with a maximum energy transfer efficiency of 38.3%. Based on the relationship between FIR and temperature, we determined that the maximum absolute sensitivity S_a and

https://doi.org/10.1021/acs.inorgchem.3c04140
Inorg. Chem. XXXX, XXX, XXX−XXX

relative sensitivity S_r for $(DA)_2PbBr_4$:0.15%Mn^{2+} are 0.055 K^{-1} and 3.207% K^{-1}, respectively. The high-temperature relative sensitivity further demonstrates the potential of $(DA)_2PbBr_4$:Mn^{2+} perovskites for optical thermometry sensor applications. This study offers a fresh perspective on the design of novel organic−inorganic hybrid perovskites, paving the way for the application of single-component, dual-emitting materials in optical thermometry sensors.

■ ASSOCIATED CONTENT

Supporting Information

The Supporting Information is available free of charge at https://pubs.acs.org/doi/10.1021/acs.inorgchem.3c04140.

Experimental section/methods, characterization, structure, and photophysical properties of $(DA)_2PbBr_4$:$x$$Mn^{2+}$ (PDF)

Accession Codes

CCDC 2325579 contains the supplementary crystallographic data for this paper. These data can be obtained free of charge via www.ccdc.cam.ac.uk/data_request/cif, or by emailing data_request@ccdc.cam.ac.uk, or by contacting The Cambridge Crystallographic Data Centre, 12 Union Road, Cambridge CB2 1EZ, U.K.; Fax: +44 1223 336033.

■ AUTHOR INFORMATION

Corresponding Authors

Lixin Ning − *Anhui Key Laboratory of Optoelectric Materials Science and Technology, Key Laboratory of Functional Molecular Solids, Ministry of Education Anhui Normal University, Wuhu 241000, China;* orcid.org/0000-0003-2311-568X; Email: ninglx@mail.ahnu.edu.cn

Zhigao Dai − *Faculty of Materials Science and Chemistry, China University of Geosciences, Wuhan 430074, China; Shenzhen Research Institute China University of Geosciences, Shenzhen 518063, China;* orcid.org/0000-0002-3105-4605; Email: daizhigao@cug.edu.cn

Guogang Li − *Faculty of Materials Science and Chemistry, China University of Geosciences, Wuhan 430074, China; Zhejiang Institute China University of Geosciences, Hangzhou 311305, China;* orcid.org/0000-0002-0523-5621; Email: ggli@cug.edu.cn

Authors

Mengyu Guan − *Faculty of Materials Science and Chemistry, China University of Geosciences, Wuhan 430074, China*

Jiarui Hao − *Department of Materials and Chemical Engineering, Taiyuan University, Taiyuan 030032, China*

Lei Qiu − *Faculty of Materials Science and Chemistry, China University of Geosciences, Wuhan 430074, China*

Maxim S. Molokeev − *Department of Physics, Far Eastern State Transport University, Khabarovsk 680021, Russia; Siberian Federal University, Krasnoyarsk 660041, Russia; Laboratory of Crystal Physics, Kirensky Institute of Physics, Federal Research Center KSC SB RAS, Krasnoyarsk 660036, Russia;* orcid.org/0000-0002-8297-0945

Complete contact information is available at: https://pubs.acs.org/10.1021/acs.inorgchem.3c04140

Notes

The authors declare no competing financial interest.

■ ACKNOWLEDGMENTS

This work was supported by the National Natural Science Foundation of China (Grant Nos. 52072349, 52172162, 12374386, and 11974022). Z.D. acknowledges support from the Fundamental Research Funds for the Central Universities, China University of Geosciences (Wuhan) (No. 162301202610), the Natural Science Foundation of Guangdong Province (2022A1515012145), and Shenzhen Science and Technology Program (JCYJ20220530162403007). G.L. acknowledges support from the Natural Science Foundation of Zhejiang Province (LR22E020004). M.M. acknowledges the support from the Ministry of Science and High Education of Russian Federation (Project No. FSRZ-2023-0006).

■ REFERENCES

(1) Zhang, F.; Park, S. Y.; Yao, C.; Lu, H.; Dunfield, S. P.; Xiao, C.; Uličná, S.; Zhao, X.; Hill, L. D.; Chen, X.; Wang, X.; Mundt, L. E.; Stone, K. H.; Schelhas, L. T.; Teeter, G.; Parkin, S.; Ratcliff, E. L.; Loo, Y.-L.; Berry, J. J.; Beard, M. C.; Yan, Y.; Larson, B. W.; Zhu, K. Metastable Dion-Jacobson 2D structure enables efficient and stable perovskite solar cells. *Science* **2022**, *375*, 71−76.

(2) Li, P.; Liang, C.; Liu, X.-L.; Li, F.; Zhang, Y.; Liu, X.-T.; Gu, H.; Hu, X.; Xing, G.; Tao, X.; Song, Y. Low-dimensional perovskites with diammonium and monoammonium alternant cations for high-performance photovoltaics. *Adv. Mater.* **2019**, *31*, No. e1901966.

(3) Guan, M. Y.; Xie, Y. L.; Zhang, Y.; Gu, Z. X.; Qiu, L.; He, Z. J.; Ye, B. K.; Suwardi, A.; Dai, Z. G.; Li, G. G.; Hu, G. W. Moisture-Tailored 2D Dion-Jacobson Perovskites for Reconfigurable Optoelectronics. *Adv. Mater.* **2023**, *35*, No. e2210611.

(4) Dai, Z. G.; Hu, G. W.; Ou, Q. D.; Zhang, L.; Xia, F. N.; Garcia-Vidal, F. J.; Qiu, C. W.; Bao, Q. L. Artificial Metaphotonics Born Naturally in Two Dimensions. *Chem. Rev.* **2020**, *120*, 6197−6246.

(5) Qiu, L.; Si, G. Y.; Bao, X. Z.; Liu, J.; Guan, M. Y.; Wu, Y. W.; Qi, X.; Xing, G. C.; Dai, Z. G.; Bao, Q. L.; Li, G. G. Interfacial engineering of halide perovskites and two-dimensional materials. *Chem. Soc. Rev.* **2023**, *52*, 212−247.

(6) Mitzi, D. B. Templating and structural engineering in organic−inorganic perovskites. *J. Chem. Soc., Dalton Trans.* **2001**, 1−12.

(7) Yu, D.; Wang, P.; Cao, F.; Gu, Y.; Liu, J.; Han, Z.; Huang, B.; Zou, Y.; Xu, X.; Zeng, H. Two-dimensional halide perovskite as beta-ray scintillator for nuclear radiation monitoring. *Nat. Commun.* **2020**, *11*, 3395.

(8) Zheng, J.; Zeng, Y.; Wang, J.; Sun, C.; Tang, B.; Wu, Y.; Zhang, Y.; Yi, Y.; Wang, N.; Zhao, Y.; Zhou, S. Hydrogen-Rich 2D Halide Perovskite Scintillators for Fast Neutron Radiography. *J. Am. Chem. Soc.* **2021**, *143*, 21302−21311.

(9) Cortecchia, D.; Mróz, W.; Neutzner, S.; Borzda, T.; Folpini, G.; Brescia, R.; Petrozza, A. Defect Engineering in 2D Perovskite by Mn(II) Doping for Light-Emitting Applications. *Chem.* **2019**, *5*, 2146−2158.

(10) Lan, N. M. C. H. P.; Huan, P. V.; Thong, N. H.; Nguyen, D.-H.; Kien, N. D. T.; Nhuong, C. M.; Thang, C. X.; Pham, V.-H. Characterization of structural and optical properties of Mn^{2+}-doped Zn_2GeO_4 nanorods as an efficient green phosphor for solid-state lighting. *Luminescence* **2022**, *37*, 577−587.

(11) Zou, S.; Liu, Y.; Li, J.; Liu, C.; Feng, R.; Jiang, F.; Li, Y.; Song, J.; Zeng, H.; Hong, M.; Chen, X. Stabilizing cesium lead halide perovskite lattice through Mn(II) substitution for air-stable light-emitting diodes. *J. Am. Chem. Soc.* **2017**, *139*, 11443−11450.

(12) Guria, A. K.; Dutta, S. K.; Adhikari, S. D.; Pradhan, N. Doping Mn^{2+} in lead halide perovskite nanocrystals: successes and challenges. *ACS Energy Lett.* **2017**, *2*, 1014−1021.

(13) Zhang, Y.; Zhao, T.; Chen, G. Recent progress in lanthanide ions doped inorganic metal halide perovskites. *J. Rare Earths* **2023**, *42*, 237−250, DOI: 10.1016/j.jre.2023.04.003.

(14) Su, B.; Molokeev, M. S.; Xia, Z. Unveiling Mn^{2+} Dopant States in Two-Dimensional Halide Perovskite toward Highly Efficient Photoluminescence. *J. Phys. Chem. Lett.* **2020**, *11*, 2510−2517.
(15) Perdew, J. P.; Burke, K.; Ernzerhof, M. Generalized gradient approximation made simple. *Phys. Rev. Lett.* **1996**, *77*, 3865−3868.
(16) Wei, Y.; Xing, G.; Liu, K.; Li, G.; Dang, P.; Liang, S.; Liu, M.; Cheng, Z.; Jin, D.; Lin, J. New strategy for designing orangish-red-emitting phosphor via oxygen-vacancy-induced electronic localization. *Light Sci. Appl.* **2019**, *8*, 15.
(17) Cortecchia, D.; Neutzner, S.; Srimath Kandada, A. R.; Mosconi, E.; Meggiolaro, D.; De Angelis, F.; Soci, C.; Petrozza, A. Broadband Emission in Two-Dimensional Hybrid Perovskites: The Role of Structural Deformation. *J. Am. Chem. Soc.* **2017**, *139*, 39−42.
(18) Smith, M. D.; Connor, B. A.; Karunadasa, H. I. Tuning the Luminescence of Layered Halide Perovskites. *Chem. Rev.* **2019**, *119*, 3104−3139.
(19) Perdew, J. P.; Ernzerhof, M.; Burke, K. Rationale for mixing exact exchange with density functional approximations. *J. Chem. Phys.* **1996**, *105*, 9982−9985.
(20) Han, D.; Shi, H.; Ming, W.; Zhou, C.; Ma, B.; Saparov, B.; Ma, Y.-Z.; Chen, S.; Du, M.-H. Unraveling luminescence mechanisms in zero-dimensional halide perovskite. *J. Mater. Chem. C* **2018**, *6*, 6398.
(21) Hills-Kimball, K.; Pérez, M. J.; Nagaoka, Y.; Cai, T.; Yang, H.; Davis, A. H.; Zheng, W.; Chen, O. Ligand Engineering for Mn^{2+} Doping Control in $CsPbCl_3$ Perovskite Nanocrystals via a Quasi-Solid−Solid Cation Exchange Reaction. *Chem. Mater.* **2020**, *32*, 2489−2500.
(22) Qiu, L.; Ju, H. N.; Guan, M. Y.; Wang, W.; Mao, W.; Dai, Z.; Li, G. G. Recycling Lead (II) Management in Metal Organic Framework-Perovskite Luminescent Composites. *Adv. Funct. Mater.* **2023**, *33*, No. 2305941.
(23) Shi, R.; Ning, L.; Wang, Z.; Chen, J.; Sham, T. K.; Huang, Y.; Qi, Z.; Li, C.; Tang, Q.; Liang, H. Zero-Thermal Quenching of Mn^{2+} Red Luminescence via Efficient Energy Transfer from Eu^{2+}in $BaMgP_2O_7$. *Adv. Opt. Mater.* **2019**, *7*, No. 1901187.
(24) Cao, R. P.; Huang, T. Y.; Nie, J. H.; Zhang, L.; Chen, Y. Y.; Li, L.; Lan, B.; Wang, J. Energy transfer and tunable-color luminescence properties of a single-phase $CaSrNb_2O_7:Sm^{3+}$, Bi^{3+}. *J. Mol. Struct.* **2024**, *1297*, No. 136962.
(25) Dang, P.; Liang, S.; Li, G.; Wei, Y.; Cheng, Z.; Lian, H.; Shang, M.; Al Kheraif, A. A.; Lin, J. Full Color Luminescence Tuning in Bi^{3+}/Eu^{3+}-Doped $LiCa_3MgV_3O_{12}$ Garnet Phosphors Based on Local Lattice Distortion and Multiple Energy Transfers. *Inorg. Chem.* **2018**, *57*, 9251−9259.
(26) Cao, R. P.; Rong, Y. T.; Cao, Y. W.; Lan, B.; Liao, C. X.; Nie, J. H.; Cheng, F. R.; Wang, J. Single- and dual-band emission $CaNb_2O_6:Mn^{2+}$: Synthesis and luminescence properties. *Mater. Res. Bull.* **2023**, *166*, No. 112344.
(27) Zhang, M. Z.; Lin, L.; Feng, Z. H.; Wang, Z. Z.; Yang, Y. M.; Ma, W. J.; Cai, J. Y.; Lu, P.; Jia, S. Y.; Zheng, Z. Q. Color-tunable hypersensitive temperature sensor based on metal organic framework doped with Eu^{3+} and Dy^{3+} via phonon-assisted energy transfer. *J. Rare Earths* **2023**, *41*, 1662−1669.
(28) Liu, D.; Yun, X.; Dang, P.; Lian, H.; Shang, M.; Li, G.; Lin, J. Yellow/Orange-Emitting $ABZn_2Ga_2O_7:Bi^{3+}$(A = Ca, Sr; B = Ba, Sr) Phosphors: Optical Temperature Sensing and White Light-Emitting Diode Applications. *Chem. Mater.* **2020**, *32*, 3065−3077.
(29) Sukul, P. P.; Mahata, M. K.; Ghorai, U. K.; Kumar, K. Crystal phase induced upconversion enhancement in Er^{3+}/Yb^{3+} doped $SrTiO_3$ ceramic and its temperature sensing studies. *Spectrochimica acta. Part A* **2019**, *212*, 78−87.
(30) Zheng, T.; Runowski, M.; Martín, I. R.; Lis, S.; Vega, M.; Llanos, J. Nonlinear Optical Thermometry—A Novel Temperature Sensing Strategy via Second Harmonic Generation (SHG) and Upconversion Luminescence in $BaTiO_3:Ho^{3+}$, Yb^{3+} Perovskite. *Adv. Opt. Mater.* **2021**, *9*, No. 2100386.
(31) Chen, D. Q.; Liu, S.; Zhou, Y.; Wan, Z. Y.; Huang, P.; Ji, Z. G. Dual-activator luminescence of RE/TM:$Y_3Al_5O_{12}$ (RE = Eu^{3+}, Tb^{3+}, Dy^{3+}; TM = Mn^{4+}, Cr^{3+}) phosphors for self-referencing optical thermometry. *J. Mater. Chem. C* **2016**, *4*, 9044−9051.
(32) Wang, C.; Lin, H.; Xiang, X.; Cheng, Y.; Huang, Q.; Gao, Y.; Cui, X.; Wang, Y. $CsPbBr_3/EuPO_4$ dual-phase devitrified glass for highly sensitive self-calibrating optical thermometry. *J. Mater. Chem. C* **2018**, *6*, 9964−9971.
(33) Xia, H.; Lei, L.; Hong, W.; Xu, S. A novel Ce^{3+}/Mn^{2+}/Eu^{3+} tri-doped GdF_3 nanocrystals for optical temperature sensor and anti-counterfeiting. *J. Alloys Compd.* **2018**, *757*, 239−245.
(34) Li, X.; Yu, Y.; Hong, J.; Feng, Z.; Guan, X.; Chen, D.; Zheng, Z. Optical temperature sensing of Eu^{3+}-doped oxyhalide glasses containing $CsPbBr_3$ perovskite quantum dots. *J. Lumin.* **2020**, *219*, No. 116897.
(35) Yu, Y.; Shao, G.; Ding, L.; Zhang, H.; Liang, X.; Liu, J.; Xiang, W. Ultra-stable Eu^{3+}-doped $CsPbCl_2Br_1$ perovskite quantum dots glass for optical temperature sensing. *J. Rare Earths* **2021**, *39*, 1497−1505.
(36) Zhang, Y.; Liu, J.; Zhang, H.; He, Q.; Liang, X.; Xiang, W. Ultra-stable Tb^{3+}: $CsPbI_3$ nanocrystal glasses for wide-range high-sensitivity optical temperature sensing. *J. Eur. Ceram. Soc.* **2020**, *40*, 6023−6030.
(37) Wu, Y. Q.; Li, J. T.; Zheng, D. Y.; Xia, X. S.; Yang, S. Q.; Yang, Y.; Bai, T. X.; Wang, X. C.; Chen, J. S.; Yang, B. Ultrasensitive Optical Thermometry via Inhibiting the Energy Transfer in Zero-Dimensional Lead-Free Metal Halide Single Crystals. *J. Phys. Chem. Lett.* **2022**, *13*, 9255−9262.

https://doi.org/10.1021/acs.inorgchem.3c04140
Inorg. Chem. XXXX, XXX, XXX−XXX